

Lattice dynamics and phase transition in CrI₃ single crystals

S. Djurdjić-Mijin,¹ A. Šolajić,¹ J. Pešić,¹ M. Šćepanović,¹ Y. Liu,²
A. Baum,^{3,4} C. Petrovic,² N. Lazarević,¹ and Z. V. Popović^{1,5}

¹*Center for Solid State Physics and New Materials, Institute of Physics Belgrade,
University of Belgrade, Pregrevica 118, 11080 Belgrade, Serbia*

²*Condensed Matter Physics and Materials Science Department,
Brookhaven National Laboratory, Upton, NY 11973-5000, USA*

³*Walther Meissner Institut, Bayerische Akademie der Wissenschaften, 85748 Garching, Germany*

⁴*Fakultät für Physik E23, Technische Universität München, 85748 Garching, Germany*

⁵*Serbian Academy of Sciences and Arts, Knez Mihailova 35, 11000 Belgrade, Serbia*

(Dated: July 10, 2018)

The vibrational properties of CrI₃ single crystals were investigated using Raman spectroscopy and were analyzed with respect to the changes of the crystal structure. All but one mode are observed for both the low-temperature $R\bar{3}$ and the high-temperature $C2/m$ phase. For all observed modes the energies and symmetries are in good agreement with DFT calculations. The symmetry of a single-layer was identified as $p\bar{3}1/m$. In contrast to previous studies we observe the transition from the $R\bar{3}$ to the $C2/m$ phase at 180 K and find no evidence for coexistence of both phases over a wide temperature range.

PACS numbers: 63.20.-e, 63.20.dk, 78.30.-j,

I. INTRODUCTION

Two-dimensional layered materials have gained attention due to their unique properties, the potential for a wide spectrum of applications and the opportunity for the development of functional van der Waals heterostructures. CrI₃ is a member of the chromium-trihalide family which are ferromagnetic semiconductors [1]. Recently, they have received significant attention as candidates for the study of magnetic monolayers. The experimental realization of CrI₃ ferromagnetic monolayers [1] motivated further efforts towards their understanding. CrI₃ features electric field controlled magnetism [2] as well as a strong magnetic anisotropy [3, 4]. With the main absorption peaks lying in the visible part of the spectrum, it is a great candidate for low-dimensional semiconductor spintronics [5]. In its ground state, CrI₃ is a ferromagnetic semiconductor with a Curie temperature of 61 K [1, 6] and a band-gap of 1.2 eV [6]. It was demonstrated that the magnetic properties of CrI₃ mono- and bilayers can be controlled by electrostatic doping [2]. Upon cooling, CrI₃ undergoes a phase transition around 220 K from the high-temperature monoclinic ($C2/m$) to the low-temperature rhombohedral ($R\bar{3}$) phase [3, 7]. Although the structural phase transition is reported to be of the first-order, it was suggested that the phases may coexist over a wide temperature range [3]. Raman spectroscopy can be of use here due to its capability to simultaneously probe both phases in a phase-separated system [8–10].

A recent theoretical study predicted the energies of all Raman active modes in the low-temperature and high-temperature structure of CrI₃ suggesting a near degeneracy between the A_g and B_g modes in the monoclinic ($C2/m$) structure. Their energies match the energies of E_g modes in the rhombohedral ($R\bar{3}$) structure [7].

In this article we present an experimental and theoretical Raman scattering study of CrI₃ lattice dynamics. In both phases all but one of the respective modes predicted by symmetry were observed. The energies for all modes are in good agreement with the theoretical predictions for the assumed crystal symmetry. Our data suggest that the first-order transition occurs at $T_s \approx 180$ K without evidence for phase coexistence over a wide temperature range.

II. EXPERIMENT AND NUMERICAL METHOD

The preparation of the single crystal CrI₃ sample used in this study is described elsewhere [11]. The Raman scattering experiment was performed using a Tri Vista 557 spectrometer in backscattering micro-Raman configuration with a 1800/1800/2400 grooves/mm diffraction grating combination. The 532 nm line of a Coherent Verdi G solid state laser was used as an excitation source. The direction of the incident light coincides with the crystallographic c axis. The sample was oriented so that its principal axis of the $R\bar{3}$ phase coincides with the x axis of the laboratory system. A KONTI CryoVac continuous Helium flow cryostat with a 0.5 mm thick window was used for measurements at all temperatures under high vacuum (10^{-6} mbar). The sample was cleaved in air before being placed into the cryostat. The obtained Raman spectra were corrected by the Bose factor and analysed quantitatively by fitting Voigt profiles to the data whereby the Gaussian width $\Gamma_{\text{Gauss}} = 1 \text{ cm}^{-1}$ reflects the resolution of the spectrometer.

The spin polarized density functional theory (DFT) calculations have been performed in the Quantum Espresso (QE) software package [12], using the Perdew-

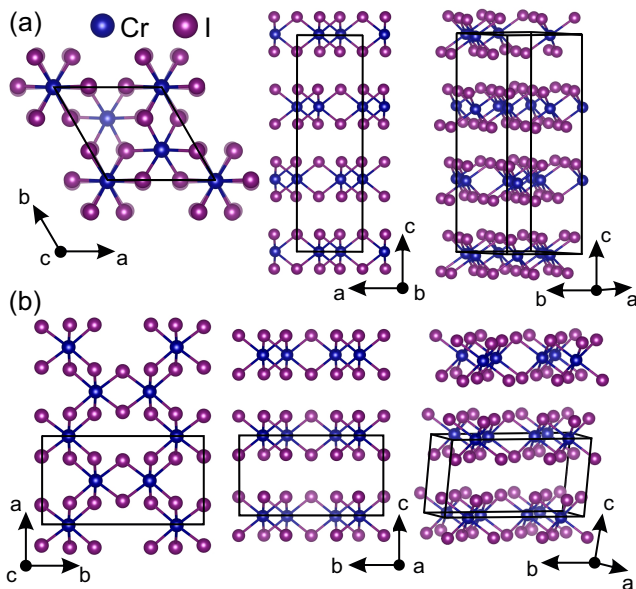


FIG. 1. (Colour online) Schematic representation of (a) the low-temperature $R\bar{3}$ and (b) the high-temperature $C2/m$ crystal structure of CrI_3 . Black lines represent unit cells.

Burke-Ernzerhof (PBE) exchange-correlation functional [13] and PAW pseudopotentials [14, 15]. The energy cut-offs for the wavefunctions and the charge density were set to be 85 Ry and 425 Ry, respectively, after convergence tests. For k -point sampling, the Monkhorst-Pack scheme was used with a $8 \times 8 \times 8$ grid centered around the Γ point. Optimization of a atomic positions in the unit cell was performed until the interatomic forces were smaller than 10^{-6} Ry/Å. To treat the van der Waals (vdW) interactions a Grimme-D2 correction [16] is used in order to include long-ranged forces between the layers, which are not properly captured within LDA or GGA functionals. This way, the parameters are obtained more accurately, especially the interlayer distances. Phonon frequencies were calculated at the Γ point using the linear response method implemented in QE. The phonon energies are compiled in Table III together with experimental values. Eigenvectors of Raman active modes for both low- and high-temperature phases are depicted in Figure A1 of the Appendix.

III. RESULTS AND DISCUSSION

CrI_3 adopts a rhombohedral $R\bar{3}$ (C_{3i}^2) crystal structure at low temperatures and a monoclinic $C2/m$ (C_{2h}^3) crystal structure at room temperature [3], as shown in Figure 1. The main difference between the high- and low-temperature crystallographic space groups arises from different stacking sequences, with CrI_3 layers being almost identical. In the rhombohedral structure the Cr atoms in one layer are placed above the center of a hole in the Cr honeycomb net of the two adjacent layers. When

TABLE I. Calculated and experimental [11] parameters of the crystallographic unit cell for the low-temperature $R\bar{3}$ and high-temperature $C2/m$ phase of CrI_3 .

$T(\text{K})$	Space group $R\bar{3}$		Space group $C2/m$	
	Calc.	Exp. [11]	Calc.	Exp. [11]
a (Å)	6.87	6.85	6.866	6.6866
b (Å)	6.87	6.85	11.886	11.856
c (Å)	19.81	19.85	6.984	6.966
α (deg)	90	90	90	90
β (deg)	90	90	108.51	108.68
γ (deg)	120	120	90	90

crossing the structural phase transition at T_s to the monoclinic structure the layers are displaced along the a direction so that every fourth layer is at the same place as the first one. The interatomic distances, mainly the interlayer distance, and the vdW gap, are slightly changed by the structural transition. The crystallographic parameters for both phases are presented in Table I. The numerically obtained values are in good agreement with reported X-ray diffraction data [11].

The vibrational properties of layered materials are typically dominated by the properties of single layers composing the crystal. The symmetry of a single layer can be described by one of the 80 dipericodic space groups (DG) obtained by lifting translational invariance in the direction perpendicular to the layer [17]. In the case of CrI_3 , the symmetry analysis revealed that the single layer structure is fully captured by the $p\bar{3}1/m$ (D_{3d}^1) dipericodic space group DG71, rather than by $R\bar{3}2/m$ as proposed in Ref. [7].

According to the factor group analysis (FGA) for the single CrI_3 layer, six modes ($2A_{1g} + 4E_g$) are expected to be observed in the Raman scattering experiment (see Table II). By stacking the layers the symmetry is reduced and, depending on the stacking sequence, FGA yields a total of eight Raman active modes ($4A_g + 4E_g$) for the $R\bar{3}$ and twelve Raman active modes ($6A_g + 6B_g$) for the $C2/m$ crystal symmetry. The correlation between layer and crystal symmetries for both cases is shown in Figure 2 (a) [18, 19].

Fig. 2(b) shows the CrI_3 single crystal Raman spectra measured at 100 K in two scattering channels. According to selection rules for the rhombohedral crystal structure (Table II) the A_g modes can be observed only in the parallel polarization configuration, whereas the E_g modes appear in both parallel and crossed polarization configurations. Based on the selection rules, peaks at about 78 cm^{-1} , 108 cm^{-1} and 128 cm^{-1} were identified as A_g symmetry modes, whereas peaks at about 54 cm^{-1} , 102 cm^{-1} , 106 cm^{-1} and 235 cm^{-1} are assigned as E_g symmetry. The weak observation of the most pronounced A_g modes in crossed polarisations [Fig. 2 (b)] is

TABLE II. Wyckoff positions of the two types of atoms and their contributions to the Γ -point phonons for the $R\bar{3}$ and $C2/m$ as well as the $p\bar{3}1/m$ diperiodic space group. The second row shows the Raman tensors for the corresponding space groups.

Space group $R\bar{3}$		Diperiodic space group $p\bar{3}1/m$		Space group: $C2/m$	
Atoms	Irreducible representations	Atoms	Irreducible representations	Atoms	Irreducible representations
Cr (6c)	$A_g + A_u + E_g + E_u$	Cr (2c)	$A_{2g} + A_{2u} + E_g + E_u$	Cr (4g)	$A_g + A_u + 2B_g + 2B_u$
I (18f)	$3A_g + 3A_u + 3E_g + 3E_u$	I (6k)	$2A_{1g} + A_{1u} + A_{2g} + 2A_{2u} + 3E_g + 3E_u$	I (4i)	$2A_g + 2A_u + B_g + B_u$
				I (8j)	$3A_g + 3A_u + 3B_g + 3B_u$
	$A_g = \begin{pmatrix} a & & \\ & a & \\ & & b \end{pmatrix}$		$A_{1g} = \begin{pmatrix} a & & \\ & a & \\ & & b \end{pmatrix}$		$A_g = \begin{pmatrix} a & & d \\ & c & \\ d & & b \end{pmatrix}$
	${}^1E_g = \begin{pmatrix} c & d & e \\ d & -c & f \\ e & f & \end{pmatrix}$		${}^1E_g = \begin{pmatrix} c & & \\ -c & d & \\ d & & \end{pmatrix}$		$B_g = \begin{pmatrix} & e & \\ e & & f \\ f & & \end{pmatrix}$
	${}^2E_g = \begin{pmatrix} d & -c & -f \\ -c & -d & e \\ -f & e & \end{pmatrix}$		${}^2E_g = \begin{pmatrix} & -c & -d \\ -c & & e \\ -d & e & \end{pmatrix}$		

TABLE III. Phonon symmetries and phonon energies for the low-temperature $R\bar{3}$ and high-temperature $C2/m$ phase of CrI_3 . The experimental values were determined at 100 K and 300 K, respectively. All calculations were performed at zero temperature. Arrows indicate the correspondence of the phonon modes across the phase transition.

Space group $R\bar{3}$				Space group $C2/m$				
Symm.	Exp. (cm^{-1})	Calc. (cm^{-1})	Calc. (cm^{-1}) [7]	Symm.	Exp. (cm^{-1})	Calc. (cm^{-1})	Calc. [7] (cm^{-1})	
E_g^1	54.1	59.7	53	\rightrightarrows	B_g^1	52.0	57.0	52
A_g^1	73.33	89.6	79	\longrightarrow	A_g^1	53.6	59.8	51
E_g^2	102.3	99.8	98	\rightrightarrows	A_g^2	78.6	88.4	79
					A_g^3	101.8	101.9	99
					B_g^2	102.4	101.8	99
E_g^3	106.2	112.2	102	\rightrightarrows	B_g^3	106.4*	108.9	101
					A_g^4	108.3	109.3	102
A_g^2	108.3	98.8	88	\longrightarrow	B_g^4	106.4*	97.8	86
A_g^3	128.1	131.1	125	\longrightarrow	A_g^5	128.2	131.7	125
A_g^4	-	195.2	195	\longrightarrow	B_g^5	-	198.8	195
E_g^4	236.6	234.4	225	\rightrightarrows	A_g^6	234.6	220.1	224
					B_g^6	235.5	221.1	225

* observed as two peak structure

attributed to the leakage due to a slight sample misalignment and/or the presence of defects in the crystal. The energies of all observed modes are compiled in Table III together with the energies predicted by our calculations and by Ref. [7] and are found to be in good agreement for the E_g modes. The discrepancy is slightly larger for the low energy A_g modes. Our calculations in general agree with those from Ref. [7]. The A_g^4 mode of the rhombohedral phase, predicted by calculation to appear at about 195 cm^{-1} , was not observed in the experiment, most likely due to its low intensity.

When the symmetry is lowered in the high-temperature monoclinic $C2/m$ phase [Fig. 2(c)] the E_g modes split into an A_g and a B_g mode each, whereas the rhombohedral A_g^2 and A_g^4 modes are predicted to switch to the monoclinic B_g symmetry. The correspondence of the phonon modes across the phase transition is indicated

by the arrows in Table III. The selection rules for $C2/m$ (see Table II) predict that A_g and B_g modes can be observed in both parallel and crossed polarization configurations. Additionally, the sample forms three types of domains which are rotated with respect to each other. We therefore identify the phonons in the $C2/m$ phase in relation to the calculations and find again good agreement of the energies. The B_g^3 and B_g^4 modes overlap and therefore cannot be resolved separately. As can be seen from the temperature dependence shown below [Fig. 4(b)] the peak at 106 cm^{-1} broadens and gains spectral weight in the monoclinic phase in line with the expectation that two modes overlap. The missing rhombohedral A_g^4 mode corresponds to the monoclinic B_g^5 mode, which is likewise absent in the spectra.

The temperature dependence of the observed phonons is shown in Figs. 3 and 4. In the low-temperature rhom-

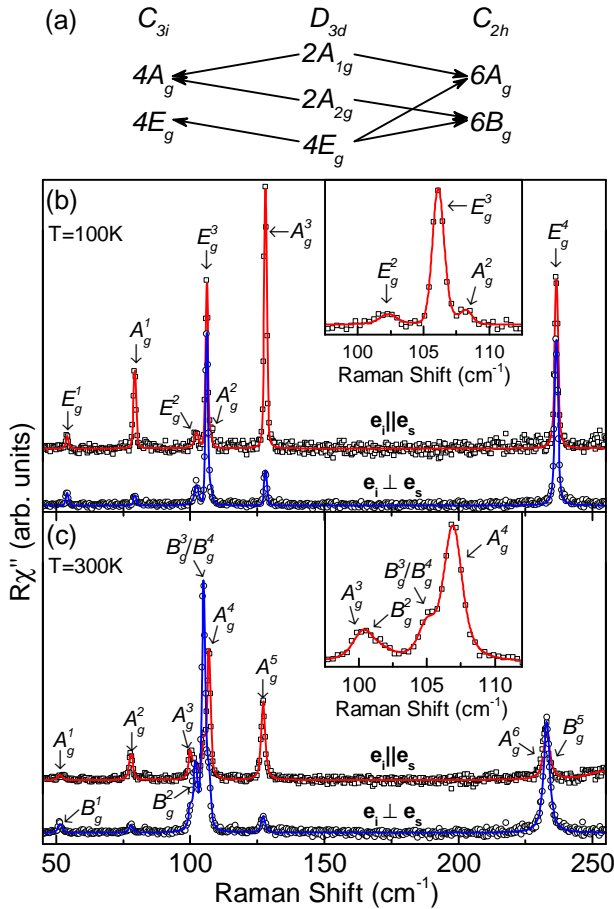


FIG. 2. (Colour online) (a) Compatibility relations for the CrI_3 layer and the crystal symmetries. Raman spectra of (b) the low-temperature $R\bar{3}$ and (c) the high-temperature $C_{2/m}$ crystal structure measured in parallel (open squares) and crossed (open circles) polarization configurations at 100 K and 300 K, respectively. Red and blue solid lines represent fits of Voigt profiles to the experimental data.

bohedral phase all four E_g modes as well as A_g^1 and A_g^2 soften upon warming, whereas A_g^3 hardens up to $T \approx 180\text{K}$ before softening again. Crossing the first order phase transition from $R\bar{3}$ to $C_{2/m}$ crystal symmetry is reflected in the spectra as a symmetry change and/or renormalization for the non-degenerate modes and lifting of the degeneracy of the E_g modes as shown in Table II. In our samples, this transition is observed at $T_s \approx 180\text{K}$. The splitting of the E_g phonons into A_g and B_g modes at the phase transition is sharp [Fig. 4]. The rhombohedral A_g^1 and A_g^3 phonons show a jump in energy and a small discontinuity in the line width at T_s [Fig. 3]. Our spectra were taken during warming in multiple runs after cooling to 100 K each time. We found that the temperature dependence for the phonon modes obtained this way was smooth in each phase. McGuire *et al.* [3, 20] reported T_s in the range of 220 K, a coexistence of both phases and a large thermal hysteresis. However, they also noted that the first and second warming cycle showed identical

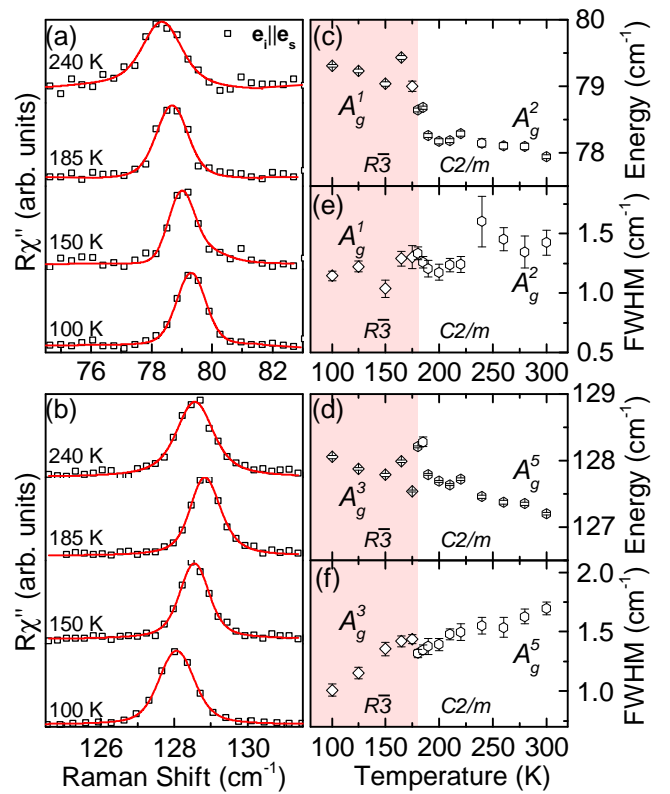


FIG. 3. (Colour online) Temperature dependence of the A_g^1 and A_g^3 phonon modes of the rhombohedral structure and the corresponding A_g^2 and A_g^5 modes of the monoclinic structure, respectively. (a,b) Raman spectra at temperatures as indicated. The spectra are shifted for clarity. Solid red lines represent Voigt profiles fitted to the data. (c,d) and (e,f) Temperature dependence of the phonon energies and line widths, respectively. Both modes show an abrupt change in energy at the phase transition at 180 K.

behaviour and only found a shift of the transition temperature to higher values of the cooling cycles. We therefore consider the difference between the reported transition around 220 K and our $T_s \approx 180\text{K}$ significant. To some extent this difference may be attributed to local heating by laser. More importantly, we find no signs of phase coexistence in the observed temperature range. The spectra for the low-temperature and high-temperature phases are distinctly different [Fig. 2] and the E_g modes exhibit a clearly resolved splitting which occurs abruptly at T_s . We performed measurements in the small temperature steps (see Figs. 3 and 4). This limits the maximum temperature interval where the phase coexistence could occur to approximately 5 K, much less than the roughly 30 to 80 K reported earlier [3, 20].

IV. CONCLUSION

We studied the lattice dynamics in the single crystalline CrI_3 using Raman spectroscopy supported by nu-

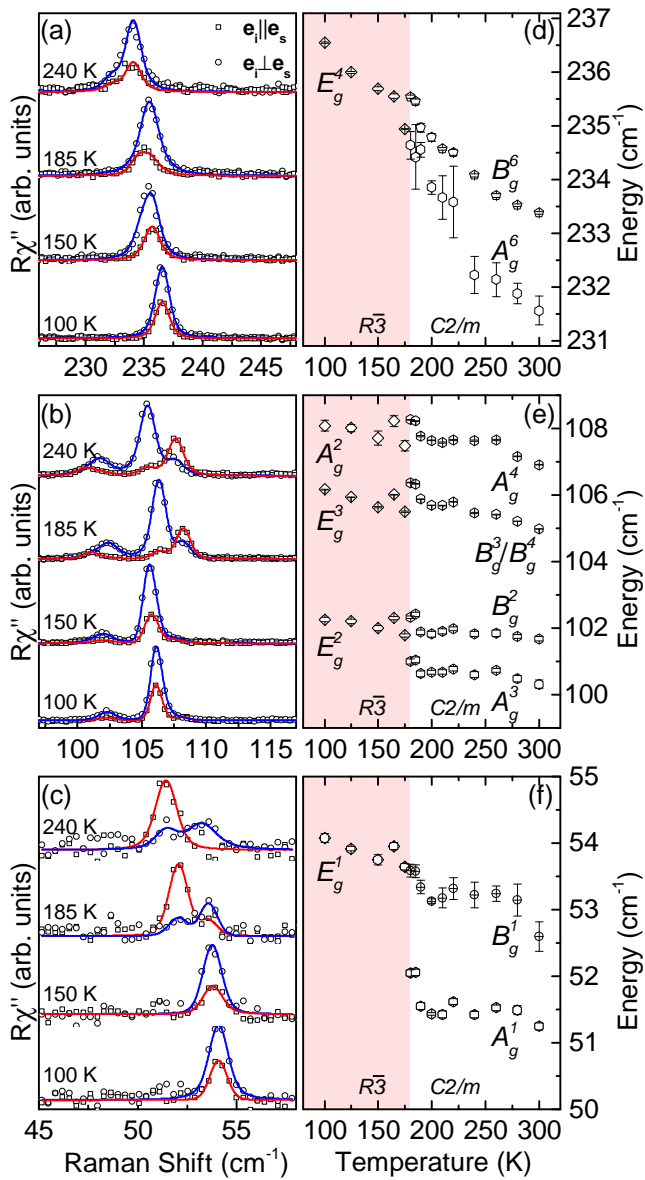


FIG. 4. (Colour online) Temperature dependence of the rhombohedral A_g^4 and E_g modes. (a-c) Raman spectra in parallel (open squares) and crossed (open circles) light polarizations at temperatures as indicated. The spectra are shifted for clarity. Blue and red solid lines are fits of Voigt profiles to the data. Two spectra were analysed simultaneously in two scattering channels with the integrated intensity as the only independent parameter. (d-f) Phonon energies obtained from the Voigt profiles. Each E_g mode splits into an A_g and a B_g mode above 180 K.

merical calculations. For both the low-temperature $R\bar{3}$ and the high-temperature $C2/m$ phases, all except one of the predicted phonon modes were identified and the calculated and experimental phonon energies were found to be in good agreement. We determined that the symmetry of the single CrI_3 layers is $p\bar{3}1/m$. Abrupt changes to the spectra were found at the first-order phase transition which was located at $T_s \approx 180$ K, lower than in previous studies. In contrast to the prior reports we found no sign of phase coexistence over temperature ranges exceeding 5 K.

ACKNOWLEDGEMENT

The work was supported by the Serbian Ministry of Education, Science and Technological Development under Projects III45018 and OI171005. DFT calculations were performed using computational resources at Johannes Kepler University, Linz, Austria. Work at Brookhaven is supported by the U.S. DOE under Contract No. DESC0012704.

[1] E. Navarro-Moratalla, B. Huang, G. Clark *et al.*, “Layer-dependent ferromagnetism in a van der Waals crystal down to the monolayer limit,” *Nature* **546**, 270–273 (2017).

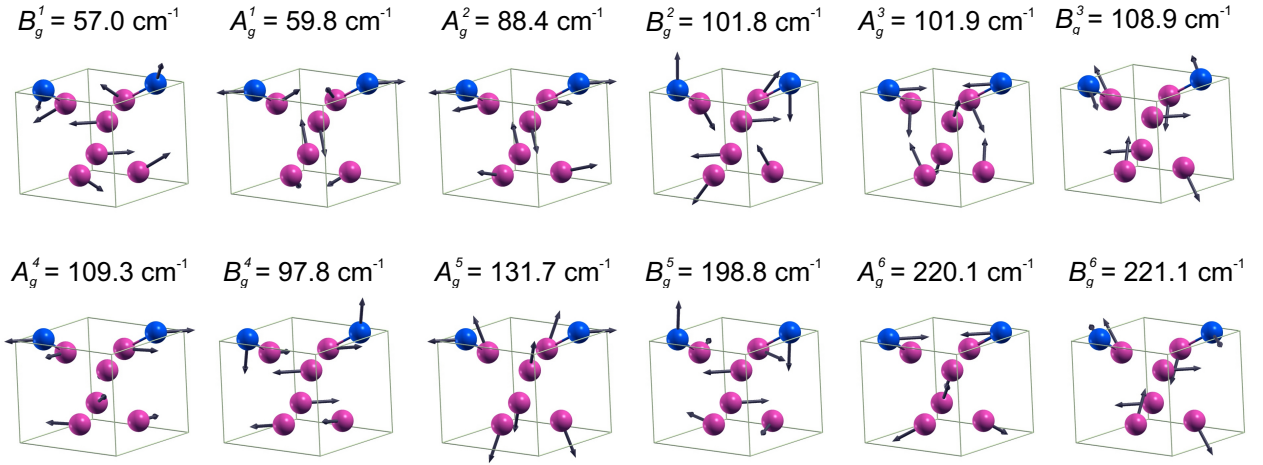
[2] Shengwei Jiang, Lizhong Li, Zefang Wang, Kin Fai Mak, and Jie Shan, “Controlling magnetism in 2D CrI_3 by electrostatic doping,” *Nat. Nanotechnol.* (2018), 10.1038/s41565-018-0135-x.

- [3] Michael A. McGuire, Hemant Dixit, Valentino R. Cooper, and Brian C. Sales, “Coupling of Crystal Structure and Magnetism in the Layered, Ferromagnetic Insulator CrI_3 ,” *Chem. Mater.* **27**, 612–620 (2015).
- [4] J. L. Ladno and J. Fernández-Rossier, “On the origin of magnetic anisotropy in two dimensional CrI_3 ,” *2D Materials* **4**, 035002 (2017).
- [5] Wei-Bing Zhang, Qian Qu, Peng Zhu, and Chi-Hang Lam, “Robust intrinsic ferromagnetism and half semiconductivity in stable two-dimensional single-layer chromium trihalides,” *J. Mater. Chem. C* **3**, 12457–12468 (2015).
- [6] J. F. Dillon Jr. and C. E. Olson, “Magnetization, resonance, and optical properties of the ferromagnet CrI_3 ,” *Chem. Mater.* **36**, 1259 (1965).
- [7] D. T. Larson and E. Kaxiras, “Raman Spectrum of CrI_3 : an ab-initio study,” ArXiv e-prints (2018), arXiv:1803.10825 [cond-mat.mtrl-sci].
- [8] N. Lazarević, M. Abeykoon, P. W. Stephens, Hechang Lei, E. S. Bozin, C. Petrovic, and Z. V. Popović, “Vacancy-induced nanoscale phase separation in $\text{K}_x\text{Fe}_{2-y}\text{Se}_2$ single crystals evidenced by Raman scattering and powder x-ray diffraction,” *Phys. Rev. B* **86**, 054503 (2012).
- [9] Hyejin Ryu, Milinda Abeykoon, Kefeng Wang, Hechang Lei, N. Lazarevic, J. B. Warren, E. S. Bozin, Z. V. Popovic, and C. Petrovic, “Insulating and metallic spin glass in Ni-doped $\text{K}_x\text{Fe}_{2-y}\text{Se}_2$ single crystals,” *Phys. Rev. B* **91**, 184503 (2015).
- [10] Hyejin Ryu, Kefeng Wang, M. Opacic, N. Lazarevic, J. B. Warren, Z. V. Popovic, Emil S. Bozin, and C. Petrovic, “Sustained phase separation and spin glass in Co-doped $\text{K}_x\text{Fe}_{2-y}\text{Se}_2$ single crystals,” *Phys. Rev. B* **92**, 174522 (2015).
- [11] Yu Liu and C. Petrovic, “Three-dimensional magnetic critical behavior in CrI_3 ,” *Phys. Rev. B* **97**, 014420 (2018).
- [12] Paolo Giannozzi, Stefano Baroni, Nicola Bonini, Matteo Calandra, Roberto Car, Carlo Cavazzoni, Davide Ceresoli, Guido L Chiarotti, Matteo Cococcioni, Ismaila Dabo, Andrea Dal Corso, Stefano de Gironcoli, Stefano Fabris, Guido Fratesi, Ralph Gebauer, Uwe Gerstmann, Christos Gougoussis, Anton Kokalj, Michele Lazzeri, Layla Martin-Samos, Nicola Marzari, Francesco Mauri, Riccardo Mazzarello, Stefano Paolini, Alfredo Pasquarello, Lorenzo Paulatto, Carlo Sbraccia, Sandro Scandolo, Gabriele Sclauzero, Ari P Seitsonen, Alexander Smogunov, Paolo Umari, and Renata M Wentzcovitch, “Quantum espresso: a modular and open-source software project for quantum simulations of materials,” *J. Phy. Condens. Mat.* **21**, 395502 (19pp) (2009).
- [13] John P. Perdew, Kieron Burke, and Matthias Ernzerhof, “Generalized gradient approximation made simple,” *Phys. Rev. Lett.* **77**, 3865–3868 (1996).
- [14] P. E. Blöchl, “Projector augmented-wave method,” *Phys. Rev. B* **50**, 17953–17979 (1994).
- [15] G. Kresse and D. Joubert, “From ultrasoft pseudopotentials to the projector augmented-wave method,” *Phys. Rev. B* **59**, 1758–1775 (1999).
- [16] Grimme Stefan, “Semiempirical GGA-type density functional constructed with a long-range dispersion correction,” *J. Comput. Chem.* **27**, 1787–1799.
- [17] Wood Elizabeth A., “The 80 diperiodic groups in three dimensions,” *Bell Syst. Tech. J.* **43**, 541–559.
- [18] W G. Fateley, Neil T. McDevitt, and Freeman F. Bentley, “Infrared and raman selection rules for lattice vibrations: The correlation method,” *Appl. Spectrosc.*, **25**, 155–173 (1971).
- [19] N. Lazarević, Z. V. Popović, Rongwei Hu, and C. Petrovic, “Evidence of coupling between phonons and charge-density waves in ErTe_3 ,” *Phys. Rev. B* **83**, 024302 (2011).
- [20] Michael A. McGuire, Genevieve Clark, Santosh KC, W. Michael Chance, Gerald E. Jellison, Valentino R. Cooper, Xiaodong Xu, and Brian C. Sales, “Magnetic behavior and spin-lattice coupling in cleavable van der Waals layered CrCl_3 crystals,” *Phys. Rev. Materials* **1**, 014001 (2017).

Appendix A: Eigenvectors

In addition to the phonon energies we also calculated the phonon eigenvectors which are shown in Fig. A1(a) for the high-temperature monoclinic phase and in Fig. A1(b) for the low-temperature rhombohedral phase. The energies, as given, are calculated for zero temperature. The relative displacement of the atoms is denoted by the length of the arrows.

(a)



(b)

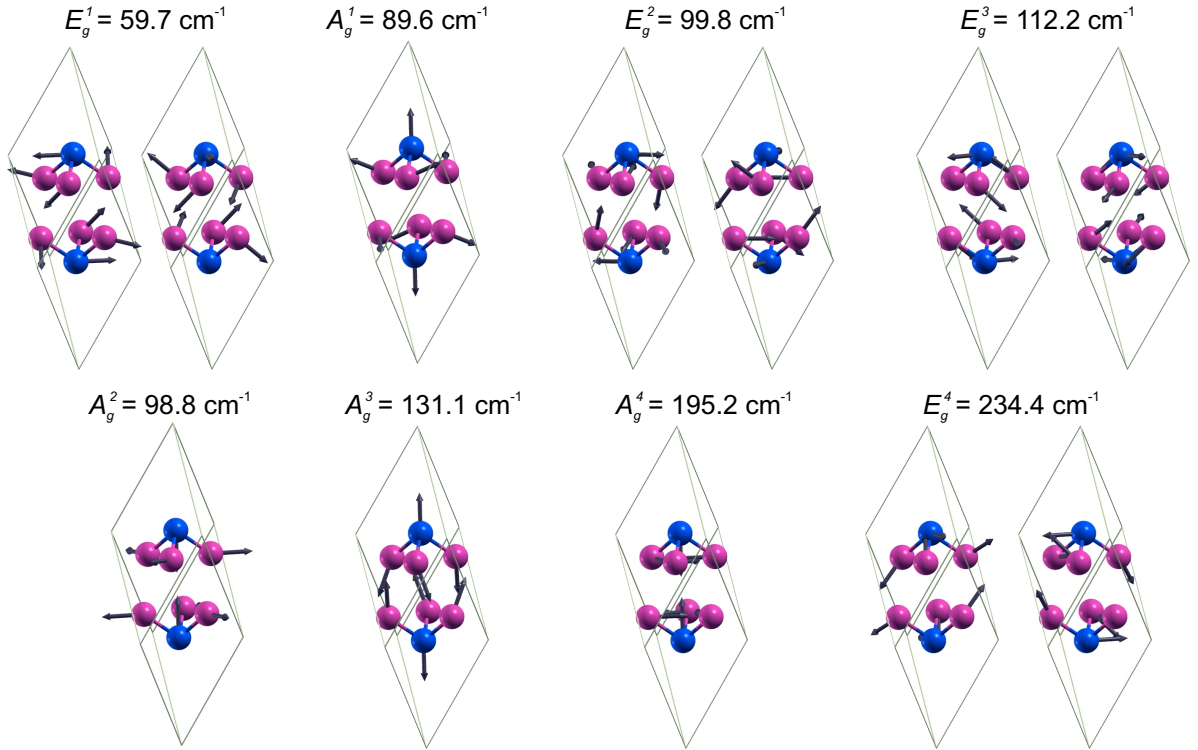


FIG. A1. Raman-active phonons in CrI_3 for (a) the monoclinic phase hosting A_g and B_g modes and for (b) the rhombohedral phase hosting A_g and E_g modes. Blue and violet spheres denote Cr and I atoms, respectively. Solid lines represent primitive unit cells. Arrow lengths are proportional to the square root of the inter-atomic forces. The given energies are calculated for zero temperature.